International Journal on Recent and Innovation Trends in Computing and Communication
ISSN: 2321-8169 Volume: 11 Issue: 11
***Article Received:** 10 September 2023 **Revised:** 20 October 2023 **Accepted:** 30 October 2023*

Advancement in Denoising MRI Images via 3D-GAN Model with Direction Coupled Magnitude Histogram Consistency Loss

A. Aaisha Nazleem[1] , Dr. S. S. Sujatha[2]

[1]Research Scholar, Reg No (17233152162001) S.T. Hindu College, affiliated to Manonmaniam sundaranar university, Nagarcoil .
[2]Principal,S.A.V Sahaya Thai Arts and Science(women) College, Vadakkankulam, Tirunelveli District.

Abstract

The diagnostics of medical pictures are essential for recognizing and comprehending a wide range of medical problems. This work introduces the Direction Coupled Magnitude Histogram (DCMH) as a novel structure picture descriptor to improve diagnostic accuracy. One of DCMH's unique selling points is its ability to include the edge oriented information that are oriented in any way inside a frame, enabling the expression of delicate nuances using various gradient features. The proposed method applies cartoon texture based textural loss and DCMH based structural loss to identify and analyse structural and textural information during the denoising time. A major contribution that improves the interpretability of images by emphasizing structural aspects that is inherent to the image. The proposed DCMH_3D_GANaverage results show exceptional performance, with an SSIM of 0.972995 and PSNR of 48.74, highlighting the effectiveness of the DCMH-based method in enhancing medical picture diagnosis. The capacity of Structured Loss to improve picture interpretability and lead to a more precise diagnosis is unquestionably advantageous. The newly developed DCMH-based approach, which includes texture loss and structured components, is a promising development in healthcare image processing that will enable better patient care through enhanced diagnostic abilities.

1. Introduction

Modern healthcare cannot function without the use of medical pictures, which are vital instruments for patient diagnosis and follow-up. One of the best medical imaging technologies is magnetic resonance imaging (MRI) [1], which uses imaging to provide extremely detailed information on the human body's live organs and tissues, including pathological and physiological changes. Two-dimensional body segments with proper tissue location, contrast, and orientation are provided by the MRI scans. Increased prediction accuracy and early diagnosis of many central nervous system disorders can be facilitated by high-resolution magnetic resonance imaging (MR) pictures with a high signal-to-noise ratio (SNR) [2-4].

Direct sampling from the spatial frequency domain yields the desired information from MRI pictures. Nevertheless, the quality of this data may be compromised by several thermal noise sources and artefacts. Because of the serious issues it raises, noise in MRIs is a serious concern that can mislead and result in patients having the wrong diagnosis. Quantitative MRI imaging is complicated by noise, which also visually deteriorates the retrieved images. Magnetic resonance imaging (MRI) is less helpful if a tissue or area has a poor signal to noise ratio (SNR). Denoising techniques are therefore needed to improve both qualitative and quantitative MRI measurements through an efficient MRI reconstruction process.

When an area or particular tissue has a poor signal to noise ratio (SNR), the efficacy of MRI falls. Consequently, an effective MRI reconstruction process is needed, where noisy images are processed using denoising algorithms to improve both quantitative and qualitative MRI measures. Since the MRI processing relies on previously processed data, noise in the data will negatively affect it. Furthermore, noise is unavoidable since it often arises throughout the MRI's recording, processing, and storing stages. Noise reduction and removal are therefore essential in this field [5]. Denoising offers a broad research potential since inadequate noise reduction can result in visual blurring or the appearance of new difficulties. Denoising offers a broad research potential since inadequate noise reduction can result in visual blurring or the appearance of new difficulties.

Medical image processing introduces a variety of MRI denoising techniques, including statistical models [6,7], spatial domain filtering [8], transform domain thresholding [9,10], isotropic diffusion methods [13], random fields [11,12], sparse representation and dictionary learning methods [14,15] and hybrid methods [16].Morphological analysis, order statistics, spatial adaptive filters, stochastic analysis, statistical estimators of all types [17], and statistical estimators of all kinds are some important additional denoising approaches[18,19]. Even though various methods for denoising have been discovered, there are several challenges that require on-going investigation, such as texture restoration and detail retention. The Generative Adversarial Network (GAN) variation used in this work has demonstrated good performance in image reconstruction challenges by using an adversarial loss to force produced pictures to be as similar to real images as feasible. The suggested method has been used to fill in the gaps in the GAN network's denoising of MRI images by including textural loss and a novel structural loss approach.

2. Related works

Medical imaging systems require the image processing task of denoising. Medical professionals may begin the required therapy by looking at noisy medical photos that have been cleaned in some way, which would increase the quality of diagnosis. Numerous studies are attempting to enhance the quality of the images by lowering the noise level. Many artificial techniques are finding success in illness detection, prediction, and image-based diagnosis very quickly.

this article presents a novel approach consisting of denoisingfol-lowed by segmentation. The objective of these proposed methods was visual eminence improvement of medical images to examine tumor extent using an adaptive partial differential equation (APDE)-based analysis with soft threshold function in denoising. The fourth order, nonlinear APDE was used to denoise the image depending on gradient and Laplacian operators associated with the new adaptiveHaar-type wavelet transform. A second approach was the new conver-gent K-means clustering for segmentation. The convergent K-means procedure diminishes the summation of the squared deviations of structures in a cluster from

A unique method that consists of segmentation after denoising was reported by Kollem et al. [20]. Using the gradient and Laplacian operators linked to the novel adaptive Haar-type wavelet transform, the picture was denoised using the fourth order, nonlinear APDE. By employing a fuzzy hexagonal membership function in conjunction with a bilateral filter, Kala et al. [21] suggested adaptive rician noise reduction that maintains fine structures and edges while enhancing denoising efficiency at varying noise variances. A texture-preserving denoising method was proposed by Zhao et al. [22]. It groups comparable texture patches using 1adaptive clustering, then applies PCA and a suboptimal Wiener filter to each group. In order to eliminate the additive white Gaussian noise, Wang et al. [23] created a fusion picture denoising filter. This filter is the result of combining the curvelet transform technique with total variation (TV).

The boundary and form of the image have been extracted using a morphological process. Three distinct filters, including the median filter, mean filter, and adaptive median filter, were used by Bin-Habtoor et al. [24] to eliminate speckle noise from medical pictures.A hybrid denoising technique based on two sparsely denoted morphological components and one residual portion was created by Zeng et al. [25] for MR images. First, use MCA to break down a noisy MR picture into its texture, cartoon, and residual portions. Next, denoise each component separately using the Wiener filter, wavelet hard threshold, and wavelet soft threshold. A fusion picture denoising filter was created by Wang et al. [26] to eliminate the additive white Gaussian noise. This filter is a combination of the curvelet transform technique and total variation (TV).

A novel BM3D [27] picture denoising method based on k-means clustering and adaptive filtering was presented by Yahya et al. [28]. Initially, the usual hard-thresholding of the BM3D filter is replaced with an adaptive filtering mechanism. The suggested adaptive filtering function is then applied using an adaptive threshold. Block matching is compelled to look inside the reference patch's boundaries by using k-means clustering, which lowers the likelihood of poor matching. To overcome the issues in BM3D, a generative adversarial network with a wiener filter and block matching with 4D filtering (BM4D) were the foundations of Zhang et al.'s [29] proposed picture denoising technique in the 3D shearlet transform domain.The BM3D and BM4D methods, however, are unable to adjust to different image contents since they both use orthogonal transformations. To enhance the denoising performance, Xu et al. [30] suggested a novel MNF–BM4D denoising method based on guided filtering. In order to discern between the main component and the noisy component, the Minimum Noise Fraction (MNF) technique is presented.

Deep learning has recently shown to be a very successful strategy in the field of medical imaging. Blan et al. [31] devised an approach that uses deep convolution and soft thresholding iterative techniques. Prior and sparse representation theory is used to get the retrieved features for picture reconstruction. DnCNN, a feed-forward denoising convolutional neural network was introduced by Zhang et al. [32] to incorporate the advancements in extremely deep architecture, learning algorithms, and regularisation techniques with Gaussian denoising. To be more precise, batch normalisation and residual learning are used to increase speed and denoising performance. An autoencoder with skip connections was put into practise by Bermudez et al. [33] Gaussian noise was used to a T1-weighted brain MRI dataset of healthy individuals in order to evaluate their methodology. In order to solve the DCE-MRI denoising issues, Benou et al. [34] introduced a unique spatio-temporal framework based on Deep Neural Networks, which was achieved by an ensemble of expert DNNs built as deep autoencoders. To reduce MRI Rician noise, Jiang et al. [35] suggested using a multi-channel approach together with residual learning and 10 convolutional layers in a neural network. For MRI image denoising, Tripathi et al. [36] suggested a unique CNN-DMRI. The network uses an encoder-decoder structure to save the image's salient elements and discard its superfluous ones.

Different Generative Adversarial Networks (GAN) models were utilised to address some of the problems with the earlier methods. To denoise compressed sensing magnetic resonance imaging, Eun et al. [37] presented CycleGAN, a cycle generative adversarial network. To eliminate motion artefacts from MRI images, Tripathi et al. [38] updated Pix2Pix, a well-known conditional Generative Adversarial Network. They adjusted the settings and made structural changes to the original network. A brand-new technique for picture denoising, called Wasserstein distance and perceptual similarity generative adversarial networks (GANs), was presented by Yang et al. [39].Using a Multi-scale Generative Adversarial Network (SMGAN), Chenyuet et al. [40] assessed the structural sensitivity of the images.

3. Proposed Work

3.1 Advancement in Medical Image Diagnosis Combining the DCMH and 3D_GAN Model

To improve medical picture diagnostics, this work presents a unique method based on a new structure image descriptor called the Direction Coupled Magnitude Histogram (DCMH). Understanding how important structural characteristics are for medical image processing, DCMH makes a special addition by including gradient and magnitude features of the slice.

Here are the main contributions:

1. Innovative DCMH Operator: By taking into consideration a different co-ordinate based gradient features to effectively preserve the structural information during the denoising process.
2. Quantitative Analysis: A way of figuring out how far apart the produced image from the original image. This research helps determine how much important structure and texture knowledge is preserved by the suggested DCMH operator along with cartoon texture pattern. This quantitative evaluation establishes the effectiveness of DCMH in gathering and preserving critical information for medical evaluation.
3. An efficient discriminator is designed for MRI denoising is presented in this model. The discriminator is designed with the squeeze-and-excitation block with residual mode and along with convolution operation. The new model of discriminator integration with DCMH offers an excellent path for improving medical picture denoising methods.

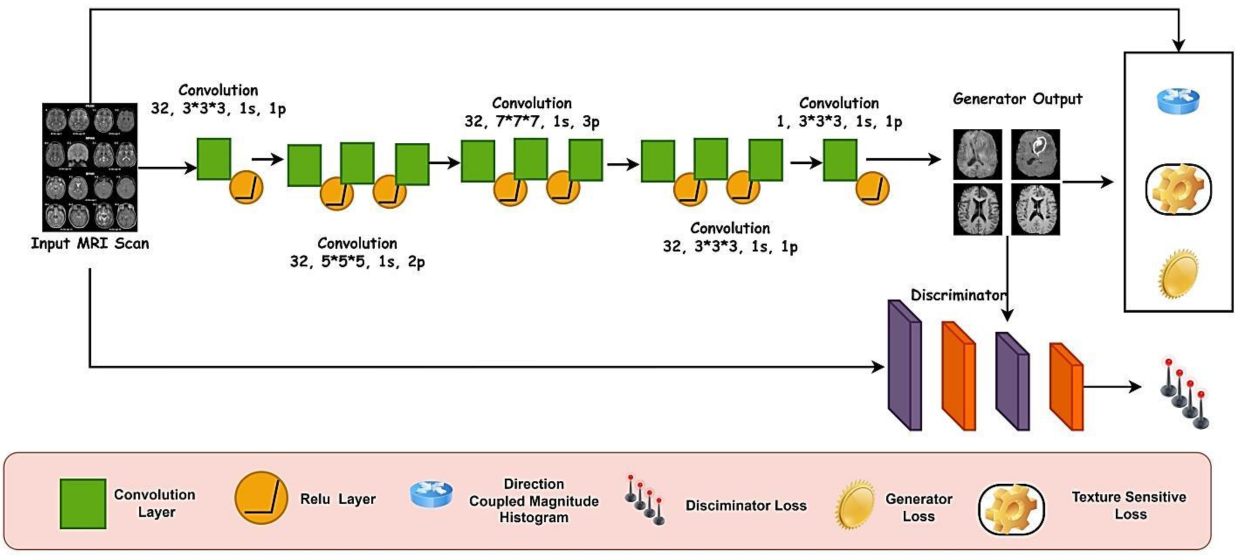

Figure 1: DCMH_GAN Workflow Architecture

International Journal on Recent and Innovation Trends in Computing and Communication
ISSN: 2321-8169 Volume: 11 Issue: 11
***Article Received:** 10 September 2023 **Revised:** 20 October 2023 **Accepted:** 30 October 2023*

The first step is giving the MRI scan as an input data of the DCMH_GAN Workflow Architecture, which is shown in Figure 1. Beginning with a convolutional layer with 32 filters, a 3x3x3 kernel size, a stride of 1, and one pixel of padding, the input is subjected to a succession of convolutional layers and ReLU activations. Then, using different kernel sizes (5x5x5, 7x7x7, and 3x3x3) and different padding, three sets of three convolutional layers and two ReLU activations are performed. The last sequence consists of a ReLU activation after a a Convolutional Layer with a single filter, 3x3x3 kernel size, stride of 1, and 1-pixel padding. An output consisting of Generator Loss, Texture Sensitive Loss, and Direction Coupled Magnitude Histogram is produced by the generator.

The Discriminator receives this Generator output as an input, which starts the Discriminator Loss computation. If the Discriminator finds differences, backpropagation is applied to the whole process. By refining the network iteratively, this feedback loop maximizes its capacity to produce outputs that meet the intended requirements. A crucial feedback mechanism in the DCMH_GAN design is formed by the interaction between the Generator and Discriminator as well as the related loss functions. This mechanism improves the DCMH_GAN architecture's ability to produce insightful results from MRI scans.

3.2 Generator

To boost textural and structural information retention while synthesizing new data from pre-existing sources, the proposed DCMH_GAN model uses a modified multi-scale 3D CNN model as its Generator (G). G is essential to the framework since it not only makes it easier to create new data but also minimizes image noise in the feature domain. The architecture, shown in Figure 2, offers a graphic depiction of the structure of the DCMH_GAN Generator, which is intended for MRI denoising. The model's capacity to generate excellent denoised images while preserving important characteristics and structures seen in the original data is enhanced by the use of this advanced generator.

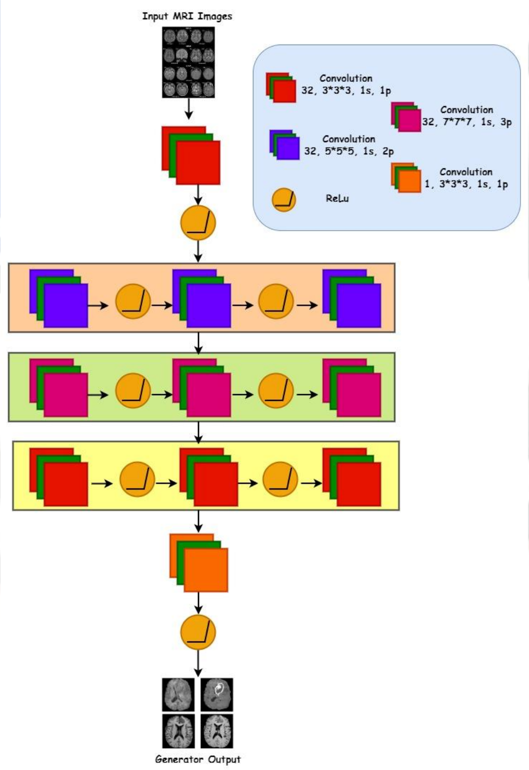

Figure 2: Generator Layer Architecture of DCMH _GAN Model

In the Figure 2, network architecture uses a generator that has several levels, each with thirty-two filters. There are five levels in the structure. The first level has a single convolutional layer with 3x3x3 filter size and one padding. On to the second level, where three convolutional layers with a padding of two and 5x5x5 filter size are used. Three convolutional layers with three pudding sand 7x7x7 filter size make up the third level. A convolutional layer with 3x3x3 filter size and one padding is introduced in the fourth level. Lastly, a convolutional layer with 3x3x3 filter size and one padding is used in the fifth level. The Rectified Linear Unit (ReLU) activation function is applied after

International Journal on Recent and Innovation Trends in Computing and Communication
ISSN: 2321-8169 Volume: 11 Issue: 11
***Article Received:** 10 September 2023 **Revised:** 20 October 2023 **Accepted:** 30 October 2023*

every convolutional process. By using different filter sizes and padding procedures at each level to increase the network's representational capacity, this hierarchical approach seeks to extract hierarchical features from the input data.

3.3 Discriminator

The Discriminator (D) network is essential to compare images that have been denoised and those that have not denoised. Its main goal is to distinguish between denoising-affected photographs and their original, undamaged equivalents. The D network provides information about the similarity between the denoised and clean images by computing a probability metric. This likelihood is a measure of how similar the two kinds of images are to one another. The discriminator layer model's architecture is illustrated graphically in Figure 3 (b), which also shows how the network is structured and how it works to discriminate across clean and denoised images.

Squeeze-and-Excitation (SE): These blocks concentrate on key characteristics to improve the performance of convolutional neural networks (CNNs) in the working model, as shown in Figure 3 (a). The "squeeze" phase in these blocks lowers computing costs by compressing spatial data. The next "excitation" phase uses channel-wise weights that have been learned to highlight pertinent characteristics. This allows the network to adaptively refocus its attention in order to optimize information flow and raise accuracy levels overall. As a result, SE blocks facilitate effective feature refinement and are essential for maximizing CNN representation capacity.

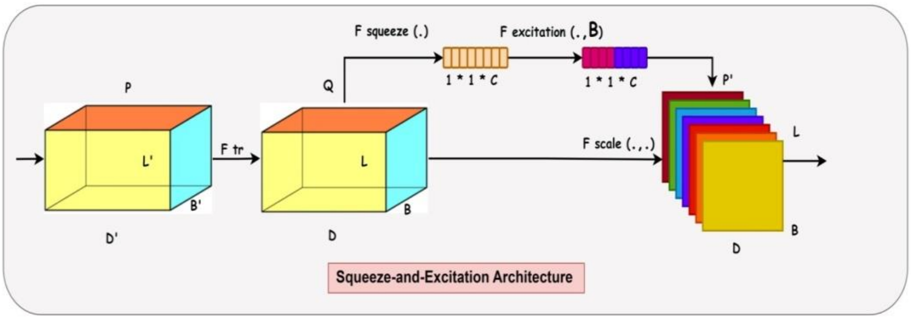

Figure 3 (a): SE Block Working Model

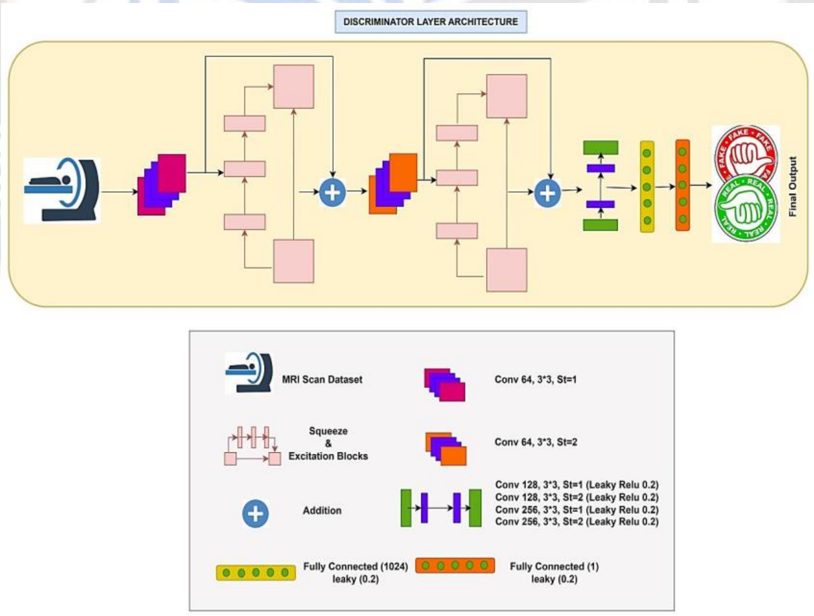

Figure 3 (b): Discriminator Layer Architecture of DCMH_GAN Model

The DCMH_GAN model's discriminator layer architecture is applied to an MRI scan dataset in Figure 3 (b). A convolutional operation using 64 filters, a 3x3 kernel, and a stride of 1 is performed in the first layer. After that, Squeeze & Excitation Blocks are used, and the output of the first convolutional layer is included in an Addition (A) operation. The procedure is then repeated with a second convolutional layer that has a stride of 2, 64 filters, and a 3x3 kernel. The feature map that is produced goes through the Squeeze & Excitation Blocks once more before being added to the accumulated value (A).

The following layers are made up of convolutional operations with different filter sizes and strides: 128 filters with a 3x3 kernel and a stride of 1 (Leaky Relu 0.2), 128 filters with a 3x3 kernel and a stride of 2 (Leaky Relu 0.2), 256 filters with a 3x3 kernel and a stride of 1 (Leaky Relu 0.2), and 256 filters with a 3x3 kernel and a stride of 2 (Leaky Relu 0.2). Next, a Fully Connected layers with Leaky Relu activation (0.2) and 1024 neurons each are deployed. The last layer consists of a Fully Connected layer with a single neuron and Leaky Relu activation (0.2), which leads to the output of the discriminator that determines if the input is real or fake.

3.4 Proposed Direction Coupled Magnitude Histogram – Structure Sensitive Loss

3.4.1 Histogram of oriented Gradient (HOG)

Histogram of Oriented Gradients [41] was initially developed by Dalal and Triggs to identify an individual in a picture. The Histogram of Oriented Gradients, often known as HOG, is a feature descriptor that counts the instances of a gradient orientation in specific areas of an image, such as the region of interest (ROI) or detection window. The images are first divided into rectangular cells by HOG. Then the gradient vector for each pixel $P_i$in the cell is computed. The following spatial filter masks are used to filter Pi in order to extract the x and y derivatives of pixels.

One option is to use more intricate spatial filter masks, such 3x3 Sobel masks.

M_x = [-1 0 1; -1 0 1; -1 0 1] $M_y = M_x^T$

Accordingly, the x derivative (Ix) and the y derivative (Iy) of Pi are calculated as Eq. 1 and 2

$$\boldsymbol{I_x(x,y,t) = \sum_{j=0}^{9} \mathbf{Mx}[j] \times P_i(x + \mathbf{Mx}[j], y, t)} \tag{1}$$

$$\boldsymbol{I_y(x,y,t) = \sum_{j=0}^{9} \mathbf{Mx}[j] \times P_i(x, y + \mathbf{Mx}[j], t)} \tag{2}$$

Equation (3) is used to calculate the gradient's magnitude (|Pi (x,y,t) | hog) and orientation (<hog Pi (x,y,t)).

$$\boldsymbol{|P_i(x,y,t)|_{hog} = \sqrt{I_x^2(x,y,t) + I_y^2(x,y,t)}}$$

$$\boldsymbol{< hogP_i(x,y,t) = arctan\frac{I_y(x,y,t)}{I_x(x,y,t)}} \tag{3}$$

The creation of histograms is the next computational step. For the [0^0, 360^0] interval, the 'a' orientation bins ({Oj}a j=1) are employed. As a result, the 'a' bins are defined as: $\boldsymbol{O_j}: \left[\frac{(j-1)360}{a}, \frac{(j)360}{a}\right]$. The matching orientation bin is located for every pixel orientation, and the orientation's magnitude is chosen to correspond to this bin using Equations (4 and 5).

$$\boldsymbol{O_j = O_j + |P_i(x,y|t)|_{hog}} \tag{4}$$

Where,

$$\boldsymbol{< hogP_i(x,y,t) \in O_j}: \left[\frac{(j-1)360}{a}, \frac{(j)360}{a}\right] \tag{5}$$

The procedure of histogram normalisation is the last phase. The histogram is normalised using the L2-norm, which produces the a-bin HOG descriptor, as shown in Eq. (6).

$$\frac{\{O_j\}_{j=1}^{a}}{\sqrt{\sum_{j=1}^{a} O_j^2}} \tag{6}$$

3.4.2 Direction coupled Magnitude Histogram

In the HOG process, the gradient vector for each pixel P_i in the cell is computed on the basis of two co-ordinates in horizontal wise as well as vertical wise. In the proposed structure consistency loss model a new form of HOG is designed with the name Direction Coupled Magnitude Histogram which generates histogram with different coordinate gradient features. The process of DCMH is expressed as follows. In this operation two more spatial filter masks of 3 × 3 in two form of diagonal arrangement as

D_{t1} = [1 0 0; 0 0 0; 0 0 -1] D_{t2} = [0 0 1; 0 0 0; -1 0 0]

Accordingly, the diagonal_1 derivative (I_{t1}) and the diagonal_1 derivative (I_{t2}) of Pi are calculated as Eq. 7 and 8.

$$\boldsymbol{I_{t1}(x,y,t) = \sum_{j=0}^{9} D_{t1}[j] \times P_i(x,y,t + D_{t1}[j])} \tag{7}$$

$$\boldsymbol{I_{t2}(x,y,t) = \sum_{j=0}^{9} D_{t2}[j] \times P_i(x,y,t + D_{t2}[j])} \tag{8}$$

Equation (9) is used to calculate the diagonal gradient's magnitude (|P_i (x,y,t) | dhog) and diagonal orientation (<dhog Pi (x,y,t)).

$$\boldsymbol{|P_i(x,y,t)|_{dhog} = \sqrt{I_{t1}^2(x,y,t) + I_{t2}^2(x,y,t)}}$$

$$\boldsymbol{< dhogP_i(x,y,t) = arctan\frac{I_{t2}(x,y,t)}{I_{t1}(x,y,t)}} \tag{9}$$

Equation (10) and (11) is used to calculate the first mode of horizontal and diagonal direction coupled $dchog_{x\_t1}$ and $dchog_{x\_t2}$. The gradient's magnitudes (|P_i (x,y,t) | $dchog_{x\_t1}$), (|P_i (x,y,t) | $dchog_{x\_t2}$) and diagonal orientations

International Journal on Recent and Innovation Trends in Computing and Communication
ISSN: 2321-8169 Volume: 11 Issue: 11
***Article Received:** 10 September 2023 **Revised:** 20 October 2023 **Accepted:** 30 October 2023*

(<dchog$_{x_t1}$ Pi (x,y,t)) , (<dchog$_{x_t2}$ Pi (x,y,t)) are estimated as follows

$$|P_i(x,y,t)|_{dchog_{x\_t1}} = \sqrt{I_x^2(x,y,t) + I_{t1}^2(x,y,t)}$$

$$< dchog_{x\_t1} P_i(x,y,t) = arctan\frac{I_{t1}(x,y,t)}{I_x(x,y,t)} \quad (10)$$

$$|P_i(x,y,t)|_{dchog_{x\_t2}} = \sqrt{I_x^2(x,y,t) + I_{t2}^2(x,y,t)}$$

$$< dchog_{x\_t2} P_i(x,y,t) = arctan\frac{I_{t2}(x,y,t)}{I_x(x,y,t)} \quad (11)$$

Similarly, The second mode of vertical and diagonal direction coupled dchog$_{y_t1}$ and dchog$_{y_t2}$ are estimated to find the correlated gradient oriented features of vertical and diagonal structural information. The following equation (12) and (13) shows the estimation of vertical and diagonal direction coupled magnitude and histogram of dchog$_{y_t1}$ and dchog$_{y_t2}$.

$$|P_i(x,y,t)|_{dchog_{y\_t1}} = \sqrt{I_y^2(x,y,t) + I_{t1}^2(x,y,t)}$$

$$< dchog_{y\_t1} P_i(x,y,t) = arctan\frac{I_{t1}(x,y,t)}{I_y(x,y,t)} \quad (12)$$

$$|P_i(x,y,t)|_{dchog_{y\_t2}} = \sqrt{I_y^2(x,y,t) + I_{t2}^2(x,y,t)}$$

$$< dchog_{y\_t2} P_i(x,y,t) = arctan\frac{I_{t2}(x,y,t)}{I_y(x,y,t)} \quad (13)$$

Once all these direction coupled magnitude and orientation estimated the final direction coupled and diagonal histogram is constructed apart from the normal HOG bin using the equations 4 and 5. Hence this proposed model extracts six different mode of histograms including, traditional hog$_{hist}$, diagonal histogram dhog$_{hist}$,horizontal and diagonal coupled histograms as (dchog$_{x_t1hist}$ and dchog$_{x_t2hist}$)and vertical and diagonal coupled histograms as (dchog$_{y_t1hist}$ and dchog$_{y_t2hist}$). The structural consistency loss is estimated with the help of Euclidian distance value between six different types of histogram derived from the actual noise free traffic data and traffic data generated by the generator.

3.5 Texture Loss - Texture Extraction (Cartoon)

The cartoon-texture algorithm breaks down any given picture I into two parts: a textural part (t) that has oscillating patterns and a cartoon component (c), where just the image's contrasting forms emerge. The low pass and high pass filter decompositions used in signal processing are equal to the decomposition I = c + t. While all frequencies, even the highest ones, are present in the cartoon section of an image due to its hard edges, a texture can also contain intermediate and high frequencies.

High total variation is the distinguishing feature of a textured region in a picture. By using a discrete convolution, two low pass filters are employed in order to calculate the gradient picture from the original image. To compute the gradient, the simplest centred difference method is employed.

The important actions are:

1. The first thing done is to apply a low pass filter to the original picture I.

   The low pass filtered image $L_\sigma * I$ is obtained by convolving the original picture I with the low pass filter $L_\sigma = (Id - (Id - G_\sigma)n)$, where n indicates that the convolution is performed n times, and n is set to 5. Gaussian kernel with standard deviation σ is denoted as G_σ.The picture is created in space with mirror boundary conditions and symmetrized out of its domain for convolutions. The present programme generates this low pass filtered picture repeatedly.

2. Determine the Euclidian norm for the image gradients of I and $L_\sigma * I$
3. The modulus of the gradient is computed using a Euclidean norm, along with the vertical and horizontal derivatives, using a centred two-point approach.

$$p_x(i,j) = p(i+1,j) - p(i-1,j) \quad (14)$$

$$p_y(i,j) = p(i,j+1) - p(i,j-1) \quad (15)$$

$$|\nabla p| = \sqrt{p_x(i,j)^2 + p_y(i,j)^2} \quad (16)$$

4. Utilising these moduli in conjunction with the Gaussian G_σ, compute the local total variation of I and$L_\sigma * I$. In space, convolutions are computed using mirror boundary conditions.
5. Find the value of λ(x) at each location in the picture.
6. By considering the weighted average of I and $L_\sigma *$ I, one may ascertain the worth of the cartoon picture.
7. Calculate the texture by dividing p by I.

Here also the textural sensitive loss is estimated with the help of the deviation between the texture feature

International Journal on Recent and Innovation Trends in Computing and Communication
ISSN: 2321-8169 Volume: 11 Issue: 11
***Article Received:** 10 September 2023 **Revised:** 20 October 2023 **Accepted:** 30 October 2023*

extracted from the actual noise free MRI slice and the generated MRI slice by the generator. Final loss is estimated with summation of generator loss, discriminator loss, cartoon texture based textural loss and Direction Coupled Magnitude Histogram(DCMH) based structural loss with the weight of 0.3, 0.3 for generator and discriminator loss and 0.2 for the textural and structural loss.

4. Experimental Analysis

4.1 Dataset

The BraTS'17 dataset, which includes multimodal MRI images for patients with pathologically confirmed diagnoses of lower-grade glioma (LGG) and glioblastoma (GBM/HGG), is used to evaluate the effectiveness of the proposed approach. The dataset is used in testing, validation, and training. In particular, T1cMRI brain DICOM images of 20 subjects were used for this investigation; each patient group had 154 slices. One-third of the photos are reserved for the testing set, while the remaining seventy percent are assigned to the training set at random. This methodology guarantees an in-depth evaluation of the model's efficacy on a range of patient data, enhancing the durability and trustworthiness of the study's outcomes.

4.2 Performance Metrics

Three important metrics to evaluate image quality are included in the performance evaluation of the proposed method: Normalized Cross-correlation (NCC), Structural Similarity Index Measure (SSIM), and Peak Signal-to-Noise Ratio (PSNR). These metrics function as all-inclusive standards to evaluate the efficacy of the suggested methodology. Together, the three metrics—PSNR, SSIM, and NCC—quantify signal fidelity, structural similarity, and normalized cross-correlation, respectively, and offer a comprehensive evaluation of the method's picture quality results. This multi-metric evaluation methodology guarantees a solid and refined comprehension of the performance of the suggested strategy in several picture quality aspects.

Peak signal-to-noise ratio (PSNR) compares two images. This ratio compares the quality of the denoised image to that of the original image.

PSNR can be determined using Equation 17.

$$PSNR = 10\log_{10}\left(\frac{MAX^2}{MSE}\right) \quad (17)$$

Where MAX indicates the Maximum Intensity Value of the image, while the Mean Square Error is MSE.

The Structural Similarity Index Measure (SSIM) is a technique for determining the perceived difference between two similar pictures. SSIM index between the two images with same size $N \times N$ can be calculated using Equation 18.

$$SSIM(x,y) = \frac{(2\mu_x\,\mu_y + c_1)(2\sigma_{xy} + c_2)}{(\mu_x^2 + \mu_y^1 + c_1)(\sigma_x^2 + \sigma_y^2 + c_2)} \quad (18)$$

Equation (19) is the Normalized Cross-correlation (NCC) formula used to compare Image 1 and Image 2. The correlation between the two images' pixel brightness is computed and normalized by their corresponding standard deviations (σ). The formula is calculating the sum of the products of the normalized pixel differences after subtracting the mean intensity of each image. Stronger similarity between the photos is indicated by a greater NCC value, which ranges from -1 (completely dissimilar) to 1 (perfectly similar).

$$\mathrm{NCC}(\mathrm{Image1}, \mathrm{Image2}) = \frac{1}{N\sigma_1\sigma_2}\sum_{x,y}(\mathrm{Image1}(x,y) - \overline{\mathrm{Image1}})x(\mathrm{Image2}(x,y) - \overline{\mathrm{Image2}}) \quad (19)$$

where N is the total number of pixels in the image, $\sigma_{1\text{ and }}\sigma_2$ are standard deviation values. Image 1 and Image 2 are NFMRI and NMRI.

4.3 Result and Analysis

By offering a strong foundation for better medical image interpretation and diagnosis, the combined use of cartoon-texture and Direction Coupled Magnitude Histogram DCMH shows a good potential to increase diagnostic skills. With its more advanced and precise toolkit for medical imaging specialists, this integrated approach has the potential to completely transform the medical imaging profession.

International Journal on Recent and Innovation Trends in Computing and Communication
ISSN: 2321-8169 Volume: 11 Issue: 11
***Article Received:** 10 September 2023 **Revised:** 20 October 2023 **Accepted:** 30 October 2023*

Table1. Denoised MRI Slices: DCMH_3D_GAN's Remarkable Enhancement Technique

Input Noise Image	De-noised Image	PSNR
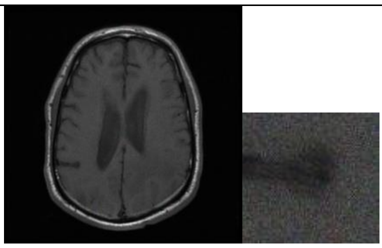	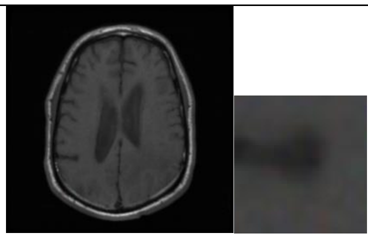	45.91
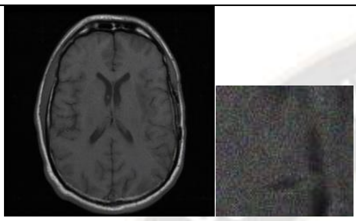	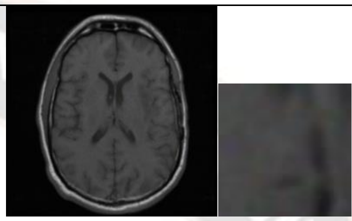	46.67
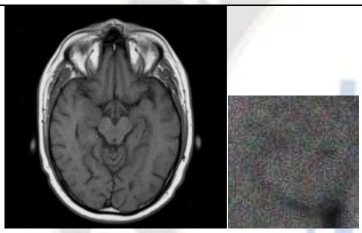	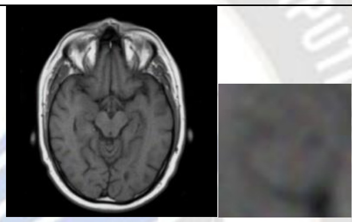	47.31
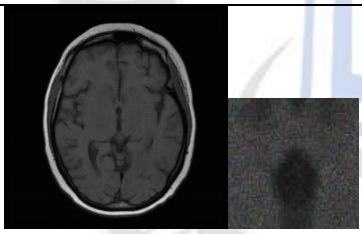	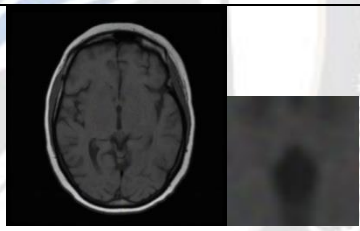	44.29

Table 1 presents denoised MRI slices achieved through the DCMH_3D_GAN method, along with corresponding Peak Signal-to-Noise Ratio (PSNR) values. These values demonstrate the method's efficacy in enhancing the quality of T1 weighted MRI DICOM images. Notably, DCMH_3D_GAN consistently outperforms other techniques, boasting the highest mean PSNR of 48.74 among SMGAN-3D, WGAN, CNN_L1, RSLM-DNN-3D, and RTSL-3D-MDNN.

Table 2. Comparative PSNR Performance of 3D Image Models

Patient ID	**1**	**2**	**3**	**4**	**5**	**6**	**Mean**
SMGAN-3D	42.82	39.03	41.8	40.47	41.55	41.63	41.21667
WGAN	40.78	37.45	39.02	38.69	40.01	40.59	39.42333
CNN_L1	37.56	38.27	37.94	36.72	37.09	37.61	37.5316
RSLM-DNN-3D	44.51	44.96	44.55	43.76	43.73	43.96	44.245
TS-3D-MDNN	46.65	46.98	46.80	44.86	45.83	44.26	45.89667
DCMH_3D_GAN	48.59	49.75	50.27	47.04	48.92	47.88	48.74166667

In Table 2, the performance of various denoising methods is evaluated based on PSNR values for T1 weighted MRI slices. SMGAN-3D, WGAN, and CNN_L1 exhibit mean PSNR values of 41.22, 39.42, and 37.53,

International Journal on Recent and Innovation Trends in Computing and Communication
ISSN: 2321-8169 Volume: 11 Issue: 11
***Article Received:** 10 September 2023 **Revised:** 20 October 2023 **Accepted:** 30 October 2023*

respectively. Meanwhile, advanced methods such as RSLM-DNN-3D and RTSL-3D-MDNN show improved performance with mean PSNR values of 44.25 and 45.90. Notably, DCMH_3D_GAN surpasses them all, achieving a remarkable mean PSNR of 48.74 and showcasing its robust denoising capabilities across multiple patient IDs.

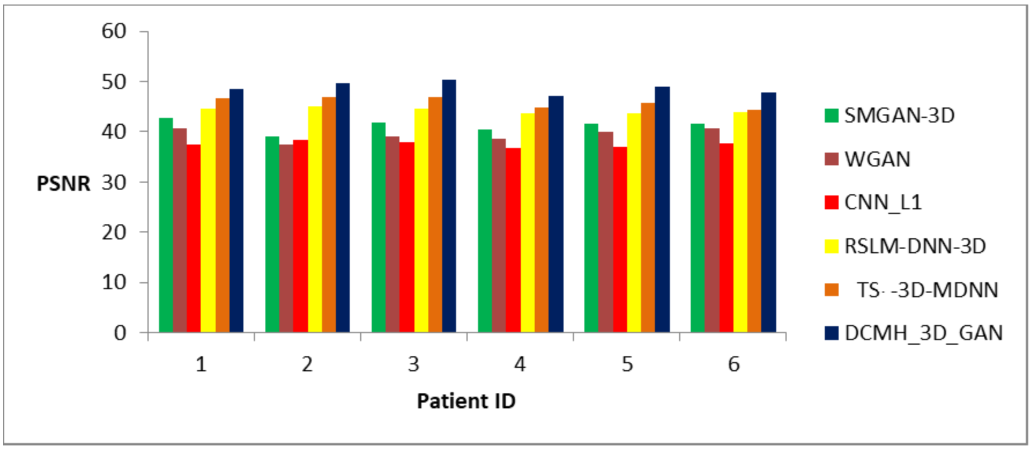

Figure4.PSNR Comparison: T1 MRI Slice Enhancement Evaluation

In the figure 4 it is found that, in terms of PSNR the average performances values of patients, our proposed DCMH_3D_GANgives better performances compared than other existing models. The proposed DCMH_3D_GAN gives average PSNR value of 2.84 higher than for TS-3D-MDNN, 4.49 for RSLM-DNN-3D, 11.21 of CNN_L1, 9.31 for WGAN and 7.52 for SMGAN-3D.The proposed DCMH_3D_GANaverage PSNR performances archives 48.74.

Table 3.SSIM Performance Comparison for 3D MRI GAN Models

Patient ID	**1**	**2**	**3**	**4**	**5**	**6**	**Mean**
SMGAN-3D	0.9802	0.97865	0.97662	0.964	0.962	0.9765	0.972995
WGAN	0.9694	0.967	0.9622	0.9532	0.9452	0.9595	0.9594167
CNN_L1	0.967	0.9601	0.95	0.944	0.94	0.954	0.9525167
RSLM-DNN-3D	0.99	0.9902	0.9899	0.983	0.984	0.98934	0.98774
TS-3D-MDNN	0.994	0.993	0.992	0.986	0.989	0.995	0.9915
DCMH_3D_GAN	0.996	0.996	0.995	0.991	0.993	0.997	0.994666667

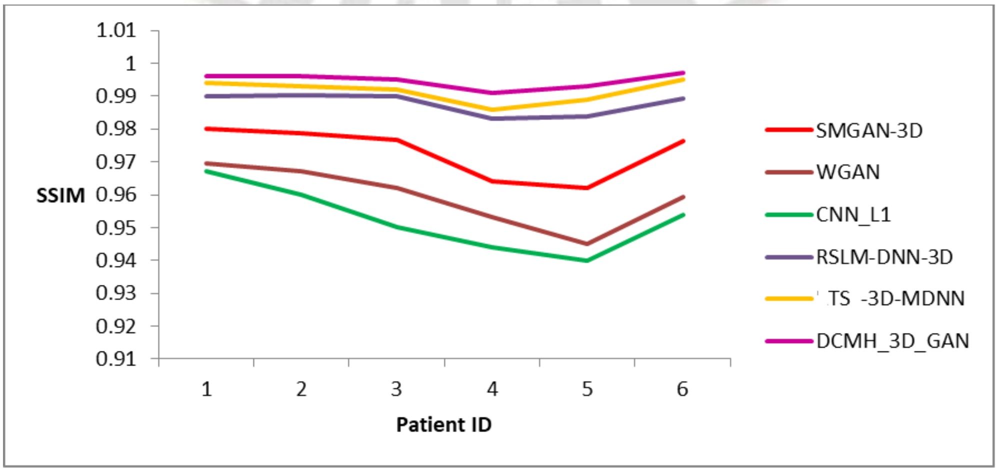

Figure 5.SSIM Comparison in T1 MRI

International Journal on Recent and Innovation Trends in Computing and Communication
ISSN: 2321-8169 Volume: 11 Issue: 11
***Article Received:** 10 September 2023 **Revised:** 20 October 2023 **Accepted:** 30 October 2023*

The performance analysis Table 3 of various models, including SMGAN-3D, WGAN, CNN_L1, RSLM-DNN-3D, TS-3D-MDNN, and DCMH_3D_GAN, based on SSIM values for T1 weighted MRI DICOM images, reveals a compelling trend. The proposed SMGAN-3D consistently demonstrates superior effectiveness, with an impressive mean SSIM value of 0.972995. This surpasses all other models, including WGAN (0.9594167), CNN_L1 (0.9525167), RSLM-DNN-3D (0.98774), TS-3D-MDNN (0.9915), and DCMH_3D_GAN (0.994666667). Notably, SMGAN-3D achieves the highest mean SSIM, indicating its robust performance in preserving structural information and image quality. Figure 5 visually reinforces this superiority, depicting the clear lead of SMGAN-3D over other models in terms of SSIM values for T1-weighted MRI DICOM images. This evidence underscores the efficacy and potential clinical relevance of the proposed SMGAN-3D model in enhancing the quality of medical imaging datasets.

Table 4. Comparative NCC Performances of 3D GANs and CNNs for T1 MRI Slices

Patient ID	**1**	**2**	**3**	**4**	**5**	**6**	**Mean**
SMGAN-3D	0.974	0.98934	0.9734	0.9688	0.9688	0.9733	0.97460667
WGAN	0.963	0.97633	0.9652	0.9633	0.9433	0.9599	0.96183833
CNN_L1	0.961	0.9574	0.9491	0.9545	0.939	0.9536	0.95243333
RSLM-DNN-3D	0.988	0.993	0.989	0.9878	0.978	0.982	0.9863
TS-3D-MDNN	0.991	0.995	0.993	0.988	0.982	0.989	0.989667
DCMH_3D_GAN	0.994	0.997	0.996	0.992	0.987	0.992	0.993

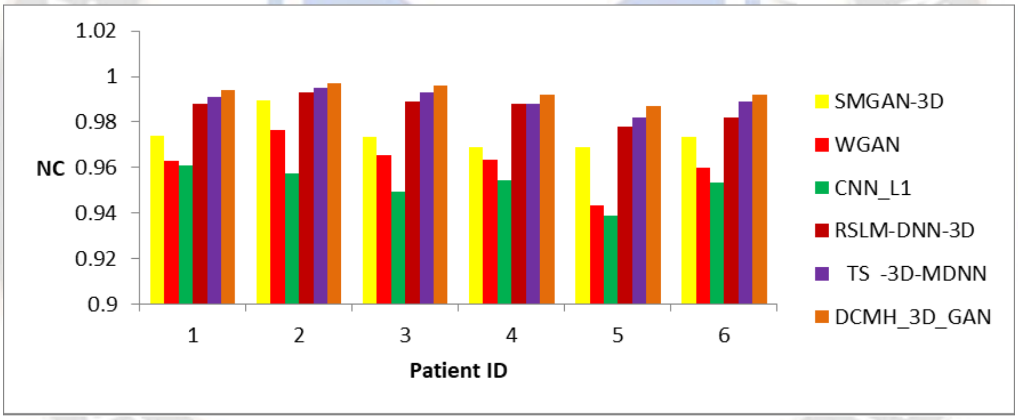

Figure 6.3D Generative Model Performance Analysis

In the evaluation of Table 4 T1-weighted MRI DICOM images, six different models, namely SMGAN-3D, WGAN, CNN_L1, RSLM-DNN-3D, TS-3D-MDNN, and DCMH_3D_GAN, were assessed based on the normalized cross-correlation (NCC) values. The mean NCC scores indicate that SMGAN-3D performed the best with a mean value of 0.9746, closely followed by RTSL-3D-MDNN at 0.9897. WGAN, CNN_L1, RSLM-DNN-3D, and DCMH_3D_GAN exhibited slightly lower mean NCC scores, highlighting variations in their performance on the T1 weighted MRI slices. Figure 6 visually depicts the performance comparison of NCC values among the models, illustrating the relative strengths and weaknesses of SMGAN-3D, WGAN, CNN_L1, RSLM-DNN-3D, TS-3D-MDNN, and DCMH_3D_GAN in the context of T1 weighted MRI image analysis.

5. Conclusion

In this paper a structure sensitive loss model is introduced along with texture sensitiveloss GAN model especially for brain MRI image denoising. A 3D-CNN with multi scale model is designed to effectively generate the noise free image. The Squeeze-and-Excitation block is adapted in the discriminator model to provide an effective feature refinement and Improves CNN representation capacity. In this work, a unique Direction Coupled Magnitude Histogram is proposed to preserve the structure information during the denoising progress. It is an enhanced version of HOG to include mixed form of oriented gradient information. The denoising model finds the textural loss with the help of cartoon texture similarity comparison. Evaluation on the BraTS'17 MRI slices proves the significant improvement in denoising parameters. The metrics such as PSNR, SSIM, and NCC are used for the evaluation process. Compared with the conventional denoising deep learning models, this DCHM with Cartoon Texture loss model with an effective discriminator module ensure the effective denoising model with the all kinds of sensitive information preserving GAN model and yields the PSNR up to 48.7. Further this approach can extend on region based sensitive denoising GAN model.

References

1. Rajeesh J, Moni RS, Palanikumar S, Gopalakrishnan T. Noise reduction in magnetic resonance images using wave atom shrinkage. International Journal of Image Processing (IJIP). 2010;4(2):131-141
2. J. Seetha and S.S. Raja, "Denoising of MRI images using filtering methods," in proc. of WiSPNET, Mar. 2016, IEEE, pp.765-769.
3. H. Rabbani, R. Nezafat, and S. Gazor, "Wavelet-domain medical image denoising using bivariate Laplacian mixture model," IEEE Transactions on Biomedical Engineering, vol.56, no.12, pp.2826-2837, 2009
4. S.M.G. Monir and M.Y. Siyal, "Denoising functional magnetic resonance imaging time-series using anisotropic spatial averaging," Biomed. Sig. Proc. and Cont., vol.4, no.1, pp.16-25, 2009.
5. S. Satheesh and K.V.S.V.R. Prasad, "Medical image denoising using adaptive threshold based on contourlet transform," Advanced Computing: An International Journal, vol.2, no.2, pp.52-58, 2011.
6. M. Kazmi, A. Aziz, P. Akhtar, A. Maftun, and W.B. Afaq, "Medical image denoising based on adaptive thresholding in contourlet domain," in proc. of ICBMEI, Oct. 2012, IEEE, pp.313-318.
7. H.M. Golshan, R.P. Hasanzadeh, and S.C. Yousefzadeh, "An MRI denoising method using image data redundancy and local SNR estimation," Magn. Reson. Imag., vol.31, no.7, pp.1206-1217, 2013.
8. S.P. Awate and R.T. Whitaker, "Nonparametric neighborhood statistics for MRI denoising," in proc. of ICIPMI, July 2005, Springer. pp. 677-688.
9. C. Pal, P. Das, A. Chakrabarti, and R. Ghosh, "Rician noise removal in magnitude MRI images using efficient anisotropic diffusion filtering," Int. J. of Imag. Sys. and Tech., vol.27, no.3, pp.248-264, 2017.
10. S.P. Awate and R.T. Whitaker, "Feature-preserving MRI denoising: a nonparametric empirical Bayes approach," IEEE Transactions on Medical Imaging, vol.26, no.9, pp.1242-1255, 2007.
11. Rajan, J. Veraart, J. Van Audekerke, M. Verhoye, and J. Sijbers, "Nonlocal maximum likelihood estimation method for denoising multiple-coil magnetic resonance images," Magnetic Resonance Imaging, vol.30, no.10, pp.1512-1518, 2012.
12. J. Rajan, J. Arnold, and J. Sijbers, "A new non-local maximum likelihood estimation method for Rician noise reduction in magnetic resonance images using the Kolmogorov–Smirnov test," Signal Processing, vol.103, pp.16-23, 2014.
13. C. Kadam and S.B. Borse, "An improved image denoising using spatial adaptive mask filter for medical images," in proc. of ICCCCA, Aug. 2017, IEEE, pp. 1-5.
14. Aslam, M. A., Munir, M. A., & Cui, D. (2020). Noise Removal from Medical Images Using Hybrid Filters of Technique. Journal of Physics: Conference Series, 1518, 012061. doi:10.1088/1742-6596/1518/1/012061
15. A.S.Y. Bin-Habtoor and S.S. Al-Amri, "Removal speckle noise from medical image using image processing techniques," Int. J. of Comp. Science and Info. Technologies, vol.7, no.1, pp.375-377, 2016.
16. Ali, H. M. (2018). MRI Medical Image Denoising by Fundamental Filters. High-Resolution Neuroimaging - Basic Physical Principles and Clinical Applications. doi:10.5772/intechopen.72427
17. M.M. Mohan, C.H. Sulochana, and T. Latha, "Medical image denoising using multistage directional median filter," in proc. of ICCPCT, Mar. 2015, IEEE, pp. 1-6.
18. Naveed, K., Akhtar,M.T., Siddiqui, M,F., &Rehman, N.,(2020), A statistical approach to signal denoising based on data-driven multiscale representation, Digital Signal Processing, 108, https://doi.org/10.1016/j.dsp.2020.102896
19. K. Naveed, B. Shaukat, S. Ehsan, K. D. Mcdonald-Maier, and N. urRehman, "Multiscale image denoising using goodness-of-fit test based on edf statistics," PloS one, vol. 14, no. 5, p. e0216197, 2019
20. M.Martin-Fernandez and S. Villullas, "The EM method in a probabilistic wavelet-based MRI denoising," Computational and Mathematical Methods in Medicine, vol.2015, pp.1-21, 2015.
21. Zhang, Y., Ding, W., Pan, Z., & Qin, J. (2019). Improved Wavelet Threshold for Image De-noising. Frontiers in neuroscience, 13, 39. Doi:10.3389/fnins.2019.00039
22. .J.V. Manjón, P. Coupé, and A. Buades, "MRI noise estimation and denoising using non-local PCA," Medical Image Analysis, vol.22, no.1, pp.35-47, 2015
23. Saito Y, Miyata T. Recovering Texture with a Denoising-Process-Aware LMMSE Filter. Signals. 2021; 2(2):286-303. https://doi.org/10.3390/signals2020019
24. Zhao, W.; Liu, Q.; Lv, Y.; Qin, B. Texture Variation Adaptive Image Denoising With Nonlocal PCA. IEEE Trans. Image Process. 2019, 28, 5537–5551.
25. Yang, J., Fan, J., Ai, D. et al. Brain MR imagedenoising for Rician noise using pre-smooth non-local means filter. BioMedEngOnLine 14, 2 (2015). https://doi.org/10.1186/1475-925X-14-2
26. Zeng Y, Zhang B, Zhao W, Xiao S, Zhang G, Ren H, Zhao W, Peng Y, Xiao Y, Lu Y, Zong Y, Ding Y. Magnetic Resonance Image Denoising Algorithm Based on Cartoon, Texture, and Residual Parts. Comput Math Methods Med. 2020 Apr 1;2020:1405647. doi: 10.1155/2020/1405647.
27. Chang, Y.-N., & Chang, H.-H. (2015). Automatic brain MR image denoising based on texture feature-based artificial neural networks. Bio-Medical Materials and

Engineering, 26(s1), S1275–S1282. doi:10.3233/bme-151425

28. A. Panda, R. Naskar, S. Rajbans and S. Pal, "A 3D Wide Residual Network with Perceptual Loss for Brain MRI Image Denoising," International Conference on Computing, Communication and Networking Technologies. pp. 1-7, doi: 10.1109/ICCCNT45670.2019.8944535.
29. A. Benou, R. Veksler, A. Friedman, and T.R. Raviv, “Ensemble of expert deep neural networks for spatio-temporal denoising of contrast-enhanced MRI sequences,” Medical Image Analysis, vol.42, pp.145-159, 2017.
30. Xie, Y. Li, H. Yang, L. Bai, T. Wang, F. Zhou, L. Zhang, and Z. Wang, “Denoising arterial spin labeling perfusion MRI with deep machine learning,” Magnetic Resonance Imaging, vol.68, pp.95-105, 2020.
31. S. Li, J. Zhou, D. Liang, and Q. Liu, “MRI denoising using progressively distribution-based neural network,” Magnetic Resonance Imaging, 2020.
32. Zhang K, Zuo WM, Zhang L (2018) FFDNet: toward a fast and flexible solution for CNN-based image denoising. IEEE Trans Image Process 27(9): 4608–4622.doi:10.1109/TIP.2018.2839891
33. Moreno López M, Frederick JM and Ventura J (2021) Evaluation of MRI Denoising Methods Using Unsupervised Learning. Front. Artif. Intell. 4:642731. doi: 10.3389/frai.2021.642731
34. Yang, H. et al. (2022). Denoising of 3D MR Images Using a Voxel-Wise Hybrid Residual MLP-CNN Model to Improve Small Lesion Diagnostic Confidence. MICCAI 2022. Lecture Notes in Computer Science, vol 13433. Springer, doi.org/10.1007/978-3-031-16437-8_28
35. Ran M, Hu J, Chen Y, Chen H, Sun H, Zhou J, Zhang Y. Denoising of 3D magnetic resonance images using a residual encoder-decoder Wasserstein generative adversarial network. Med Image Anal. 2019 Jul;55:165-180. doi: 10.1016/j.media.2019.05.001.
36. Zhang, K.; Zuo, W.; Chen, Y.; Meng, D.; Zhang, L. Beyond a Gaussian Denoiser: Residual Learning of Deep CNN for Image Denoising. IEEE Trans. Image Process. 2017, 26, 3142–3155
37. D. Jiang, W. Dou, L. Vosters, X. Xu, Y. Sun, and T. Tan, “Denoising of 3D magnetic resonance images with multi-channel residual learning of convolutional neural network,” Japanese Journal of Radiology, vol.36, no.9, pp.566-574, 2018.
38. A. AaishaNazleem, Dr. S.S. Sujatha., Texture and Structure Sensitive 3D Multi-scale Deep Neural Network for MR Images Denoising. Journal of Survey in Fisheries Sciences. Vol.10 No. 3s(2023). Doi:doi.org/10.17762/sfs.v10i3S.119
39. Yang, Q., Yan, P., Zhang, Y, Yu, H., Shi, Y., Mou, X., Kalra, M K.,&. Wang, G (2017), “Low dose CT image denoising using a generative adversarial network with wasserstein distance and perceptual loss,” arXiv preprint arXiv:1708.00961
40. ZhiPing, Q.,YuanQi, Z., Yi, S.,&Xiangbo, L. (2018). A New Generative Adversarial Network for Texture Preserving Image Denoising. 1-5. 10.1109/IPTA.2018.8608126